AGU PUBLICATIONS

JGR

Journal of Geophysical Research: Solid Earth

RESEARCH ARTICLE

10.1002/2013JB010601

Key Points:
- Crustal seismic attenuation measured in the Himalaya
- V_P/V_S and Q in the Tibetan midcrust attributed to alpha-beta quartz transition
- Underthrusting Indian Plate marked by high Q and high seismic wave speeds

Supporting Information:
- Readme
- Figure S1
- Figure S2

Correspondence to:
Anne F. Sheehan,
Anne.Sheehan@colorado.edu

Citation:
Sheehan, A. F., T. L. de la Torre, G. Monsalve, G. A. Abers, and B. R. Hacker (2014), Physical state of Himalayan crust and uppermost mantle: Constraints from seismic attenuation and velocity tomography, *J. Geophys. Res. Solid Earth*, *119*, 567–580, doi:10.1002/2013JB010601.

Received 12 AUG 2013
Accepted 16 DEC 2013
Accepted article online 27 DEC 2013
Published online 29 JAN 2014

Physical state of Himalayan crust and uppermost mantle: Constraints from seismic attenuation and velocity tomography

Anne F. Sheehan[1], Thomas L. de la Torre[1,2], Gaspar Monsalve[1,3], Geoffrey A. Abers[4], and Bradley R. Hacker[5]

[1]Cooperative Institute for Research in the Environmental Sciences and Department of Geological Sciences, University of Colorado Boulder, Boulder, Colorado, USA, [2]Now at Tricon Geophysics, Inc., Denver, Colorado, USA, [3]Now at Facultad de Minas, Universidad Nacional de Colombia sede Medellín, Medellín, Colombia, [4]Lamont Doherty Earth Observatory, Columbia University, Palisades, New York, USA, [5]Department of Earth Science, University of California, Santa Barbara, California, USA

Abstract We jointly interpret P and S wave seismic attenuation ($1/Q$) along with previously published seismic velocity results for the crust and uppermost mantle of eastern Nepal and the southern Tibetan Plateau. Seismic attenuation measurements can provide information complementary to seismic velocity estimates and can help distinguish between compositional and thermal mechanisms for observed anomalies. In addition to a dramatic change in seismic velocity observed between the crust of Nepal and southern Tibet, we find a large increase in seismic attenuation from high Q (low attenuation) in eastern Nepal to low Q (high attenuation) in the crust beneath southern Tibet for both P waves and S waves. We interpret the broad zone of low Q values in the southern Tibetan crust as thermal in origin, requiring an elevated geotherm (warm) relative to Nepal, with low V_P/V_S corresponding to a dominantly felsic middle and upper crust beneath southern Tibet. We find a sharply bounded region with enhanced low Q and high V_P/V_S at 45–50 km depth beneath southern Tibet, which we suggest may be due to trapped fluid beneath an impermeable cap associated with the crustal alpha-beta quartz transition. Using calibrations from mineral physics, the alpha-beta quartz transition suggests a temperature of 930–960°C at 45 km depth (50 km beneath the surface) beneath the southern Tibetan Plateau. High values of Q_P and Q_S throughout the uppermost mantle in the region are consistent with cool temperatures in the underthrusting Indian Plate, contributing to brittle conditions and earthquakes in the uppermost mantle.

1. Introduction and Background

The lithospheric structure of the Himalaya and the Tibetan Plateau—major features of continental collision between India and Eurasia—is key for understanding the mechanisms that accompany and control deformation of the continental lithosphere. Phase transformations, in particular melting, play important roles in determining the rheology of the upper lithosphere in regions of continental collision. The Himalaya of Central Nepal and the southernmost Tibetan Plateau are regions where this type of collision is ongoing, and processes active within the underthrusting Indian Plate can be evaluated using seismological techniques (Figure 1).

India and southern Tibet are converging at an approximate rate of 20 ± 3 mm/yr [*Larson et al.*, 1999], resulting in crust greater than 70 km thick [*Zhao et al.*, 1993; *Schulte-Pelkum et al.*, 2005; *Priestley et al.*, 2008]. The Himalayan Chain has formed as a result of crustal thickening and is composed largely of buried and exhumed Indian crust [*Molnar*, 1984]. The convergence has been absorbed chiefly by thrusting along major fault zones, with a southward progression of thrusting [*Gansser*, 1964; *DeCelles et al.*, 2001; *Robinson et al.*, 2003]. The southern limit of the Himalayan Chain is defined by the Main Frontal Thrust; the boundary between India and Eurasia is the Indus-Tsangpo suture zone [*Hodges*, 2000].

Leucogranites exposed in the Himalaya formed mostly during Eocene-Miocene partial melting of Indian crust during the collision [*Molnar*, 1984; *Beaumont et al.*, 2004]. Geophysical studies support the existence of a partially molten or aqueous fluid-rich layer in the middle and lower crust beneath southern Tibet and the Himalaya today [*Nelson et al.*, 1996; *Unsworth et al.*, 2005; *Klemperer*, 2006; *Caldwell et al.*, 2009]. These ancient and active features have been linked by tectonic models in which midcrustal material flows out from beneath the plateau and is exhumed [*Nelson et al.*, 1996; *Clark and Royden*, 2000; *Beaumont et al.*, 2004]. Thus, although collision should thicken the crust and reduce geothermal gradients, processes must exist to heat it and

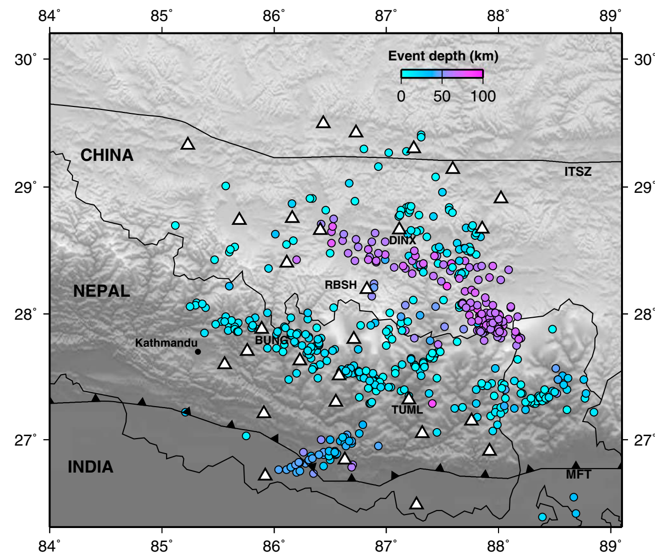

Figure 1. Grey scale shaded relief map showing Himalayan Nepal Tibet Seismic Experiment (HIMNT) broadband seismograph stations (white triangles) and earthquakes used in attenuation study (circles, colored by depth). See Figure S1 for path coverage. Station code is given for seismographs referenced in the text (TUML, BUNG, DINX, and RBSH). MFT: Main Frontal Thrust; ITSZ: Indus Tsangpo Suture Zone. Station RBSH (28.195°N, 86.828°E) is used as the center point (distance = 0 in cross sections) for the tomographic models. Ray coverage is shown in Figure S1.

support melting as well as enhance crustal flow. An evaluation of the physical state of the upper lithosphere across the Himalayan Chain and southernmost Tibet will help us deduce the presence or absence of fluids, the dimensions over which they are distributed, and the properties of the host rock.

There is evidence for the occurrence of earthquakes below the seismically defined Moho beneath the High and Tethyan Himalaya [*Chen and Molnar*, 1983; *Chen and Yang*, 2004; *Schulte-Pelkum et al*., 2005; *Monsalve et al*., 2006], indicating that the continental uppermost mantle must provide part of the strength to support the mountain and plateau loads and that the underthrusting Indian Plate beneath the southern edge of the Tibetan Plateau should be cold enough to allow brittle failure. In this paper we summarize the measurement of seismic attenuation using local earthquakes recorded on a temporary seismic network in eastern Nepal and southern Tibet, with special emphasis on interpretation along with a previously published seismic velocity model. We utilize the complementary nature of the attenuation and velocity models in order to better constrain the physical state of the crust and upper mantle beneath the Himalaya.

2. Instruments and Data

The Himalayan Nepal Tibet Seismic Experiment (HIMNT) included the deployment of 30 broadband seismometers throughout eastern Nepal and Southern Tibet from October 2001 to March 2003 [*de la Torre and Sheehan*, 2005; *Sheehan et al*., 2008]. The stations were deployed in a 2-D grid with an approximate spacing of 50 km. Each station consisted of a three-component Streckheisen STS2 broadband seismometer, and data were recorded continuously at 40 or 50 samples per second. Over 1600 earthquakes ranging from magnitude 1 to 5.5 were located using the HIMNT data [*Monsalve et al*., 2006]. For the attenuation study the earthquake database was restricted to events that were well recorded by at least six stations, had magnitude $> 2.0\, M_L$ and had signal-to-noise ratio of at least 1.5. Two hundred and forty earthquakes out of the 1649 cataloged in *Monsalve et al*. [2006] met these strict criteria. The majority of the 240 earthquakes occurred at depths of 10–30 km along the Himalayan Arc and in the southern Tibetan Plateau and at depths $>$ 50 km in a cluster beneath the High Himalaya in the center of the network (Figure 1).

3. Attenuation Measurements

Strong variations in spectral character are observed in the raw HIMNT waveforms (Figure 2). To quantify these spectral variations, *P* and *S* waveforms from local events recorded by the HIMNT array were analyzed for attenuation and source effects following the method of *Stachnik et al*. [2004]. After removing the instrument response and converting the seismograms from velocity to displacement, we determine amplitude as a function of

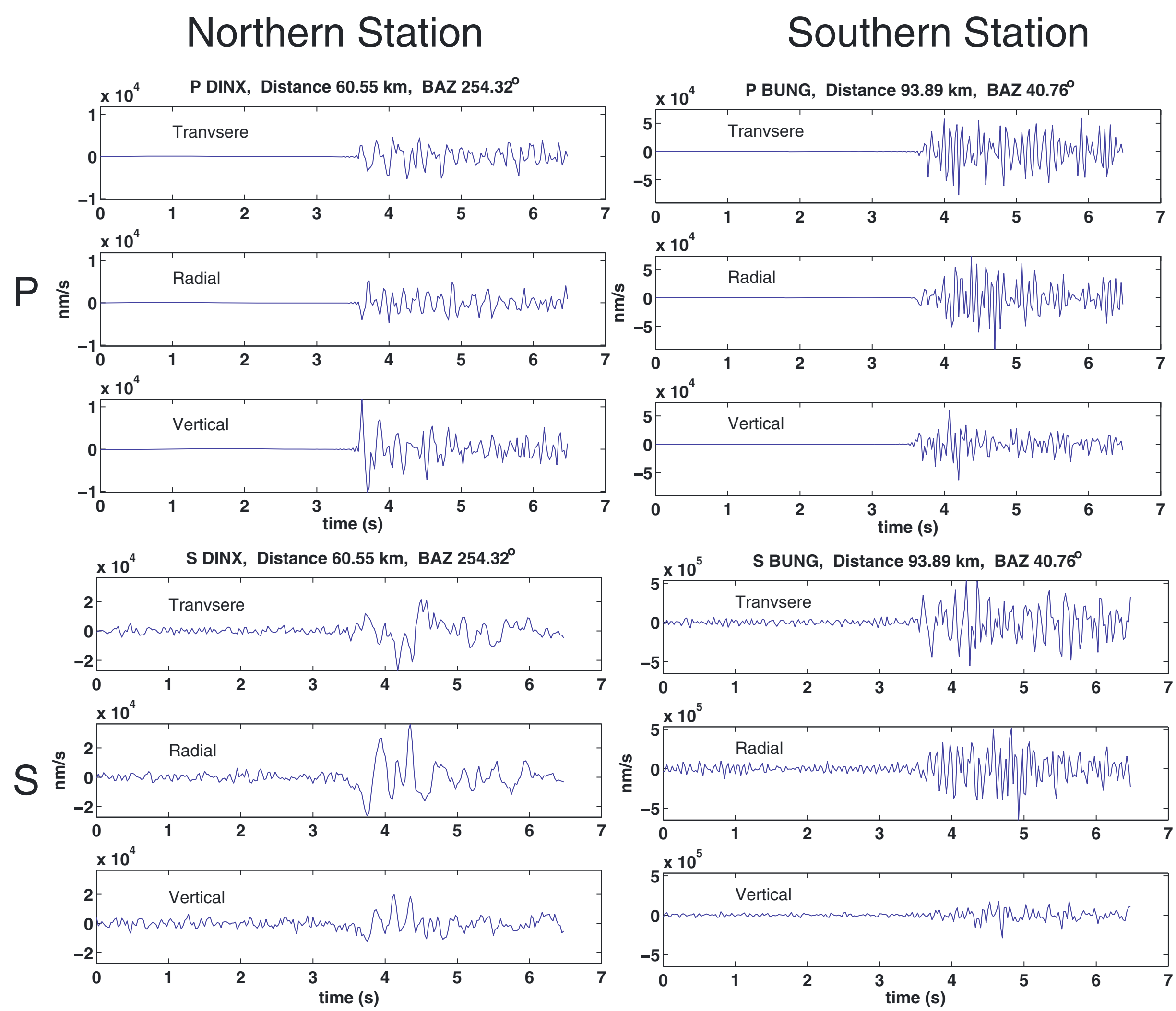

Figure 2. Example (top) *P* and (bottom) *S* wave seismograms from 8 May 2002 M_w 3.7 earthquake, located at 28.51°N, 86.51°E, 84 km depth beneath the High Himalaya and recorded at (left) seismic station DINX in southern Tibet (labeled "Northern Station") and (right) seismic station BUNG in Nepal (Southern Station). All records are 7 s long. Window for spectral measurement is 3 s in duration and begins 0.5 s before the arrival. Vertical component is used for *P* wave spectral measurement and transverse component is used for *S* wave spectral measurement. Vertical scale varies by trace. Data from the northern station, despite being closer to the earthquake, have smaller amplitudes than those from the southern station and are depleted in high frequencies relative to the southern station. STS2 seismometers were used in each case.

frequency f, $A(f)$, via a multitaper spectral analysis [*Park et al.*, 1987; *Boyd and Sheehan*, 2005] for each seismogram using a 3 s long window beginning 0.5 s before the *P* arrival on the vertical component or the *S* arrival on the transverse component (Figure 3). A similarly processed noise spectrum is generated using a 3 s time window ending 0.5 s before the phase arrival. Most of the *P* and *S* wave energy used in this study corresponds to crustal *Pg* and *Sg* phases. Event-station pairs for which *Pn* is the first arrival, or *Sn* is the first shear wave arrival, should represent less than 10% of the data. When that is the case, *Pg* or *Sg* should take up most of the energy in the time window used here, given that the epicentral distances are within a few tens of kilometers from the cross-over distance where *Pg* and *Sg* are still large. Only frequencies with signal spectrum exceeding the noise spectrum are used in measuring source and attenuation parameters. On average, for *P* waves the frequency band of the measurements was 1.0–13.1 Hz, whereas for *S* waves it was 0.7–11.2 Hz. Following *Stachnik et al.* [2004], we assume that the observed displacement spectrum $A(f)$ for each event-station pair can be represented by

$$A(f) = \frac{CM_0 \exp(-\pi f t^*)}{1 + (f/\mathrm{fc})^2} \tag{1}$$

where Mo is seismic moment of the earthquake, fc is the source corner frequency, t^* is phase travel time divided by the attenuation factor Q along the raypath, and C accounts for frequency-independent source

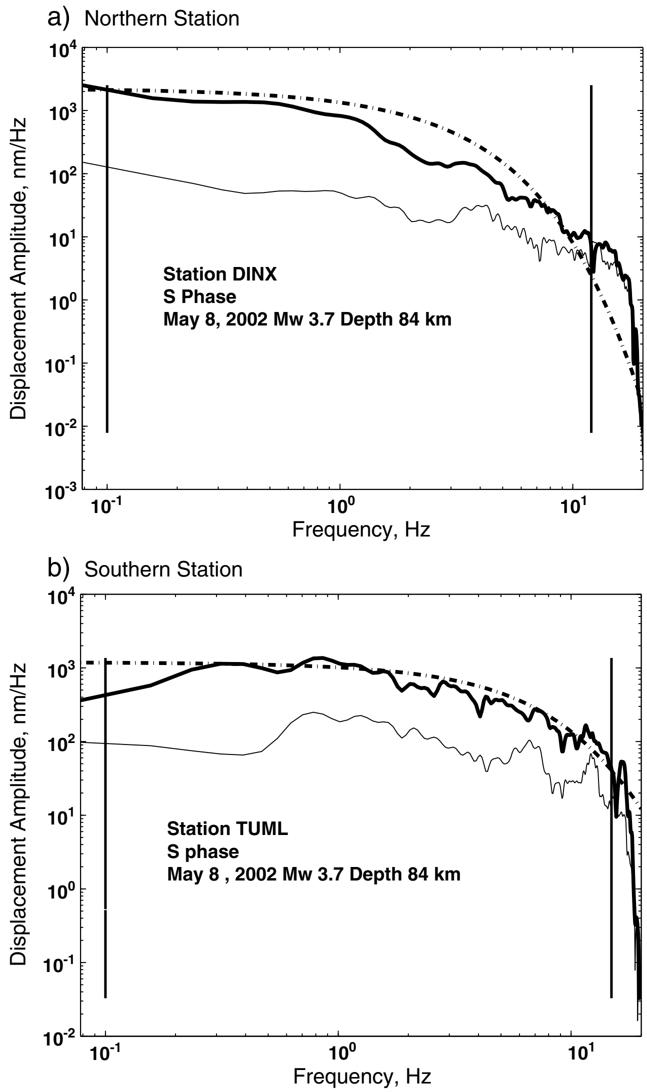

Figure 3. *S* wave spectra of the event shown in Figure 2, from (a) Tibet station DINX and (b) Nepal station TUML. Solid vertical lines denote the frequency ranges at which the spectra were modeled. Dashed line shows best fit model following equation 1. Note a lack of high-frequency energy at DINX, typical of northern paths. Assuming similar source spectra at both stations, the faster decay of the shear wave spectra toward higher frequencies in Figure 3a indicates a higher t^* (higher attenuation) for the northern path compared to that for the southern path.

excitation and propagation effects such as geometrical spreading [*Aki and Richards*, 2002]. Taking the natural logarithm of equation (1) and rearranging terms gives

$$\ln(A(f)) + \ln\left(1 + (f/\mathrm{fc})^2\right) - \ln(C) = \ln(\mathrm{Mo}) + (-\pi f)t^*. \tag{2}$$

A system of equations of this form are solved simultaneously at all frequencies for all stations recording a single event and phase (*P* or *S*), to determine a single fc and Mo for each event and a separate t^* for each event-station pair. *C* is calculated with the same approach as that used by *Stachnik et al*. [2004]. The equations are linear in t^* and ln(Mo) but nonlinear in fc. A grid search is performed over fc values from 0.25–50 Hz at 0.25 Hz intervals, and at each fc the Mo and t^* are found by weighted least squares inversion. The fc producing the smallest misfit is chosen, with corresponding Mo and t^*. The average of resulting fc values was 18.4 Hz for *P* waves and 14.1 Hz for *S* waves. The moments (Mo) obtained from this method are positively correlated but biased low compared to the moments obtained from full waveform moment tensor inversion [*de la Torre et al*., 2007] (Figure 4). Source parameters are determined separately for *P* and *S*, because fc may differ with phase [e.g., *Madariaga*, 1976].

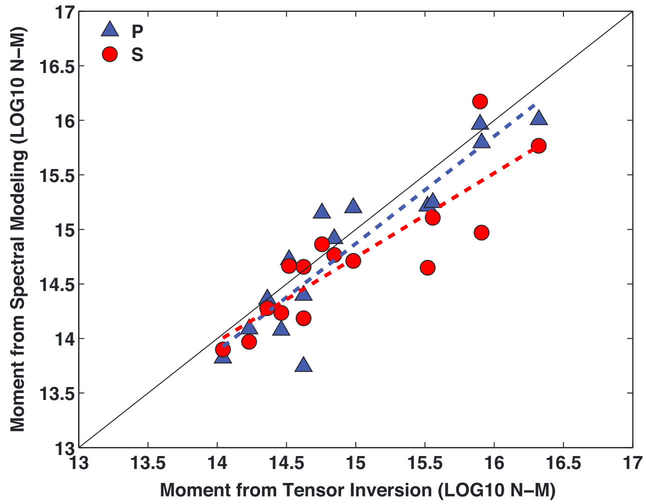

Figure 4. Seismic moment (N-m) from spectral modeling (this paper) versus seismic moment from moment tensor inversion [*de la Torre et al.*, 2007] for 15 earthquakes common to both studies. Dashed lines represent best fit between spectral modeling and moment tensor derived seismic moment for *P* waves (blue) and *S* waves (red). Solid diagonal line represents 1:1 ratio.

We assume here that the attenuation Q is independent of frequency f. Many laboratory and observational studies have shown that Q increases weakly with frequency at mantle conditions [e.g., *Karato and Spetzler*, 1990; *Flanagan and Wiens*, 1998]. Laboratory studies of melt-free olivine-dominated rocks show that Q increases as $f^{0.2\text{–}0.3}$ [e.g., *Faul and Jackson*, 2005], but comparable studies have not been done on crustal rocks. Many studies of seismic wave propagation in continental crust show stronger frequency dependence in tectonically active areas ($Q \sim f^{0.4\text{–}0.7}$) [*Mitchell*, 1995], and significant bulk modulus attenuation (indicated by $Q_P/Q_S < 1$) [e.g., *Singh et al.*, 2012; *Hazarika et al.*, 2013] unlike the laboratory studies, making it difficult to directly apply laboratory studies of high-temperature mantle rocks to our crustal study, even with corrections for homologous temperature. Moreover, some of these crustal observations of frequency dependence have been called into question as a potential effect of incorrect geometric spreading corrections [*Morozov*, 2009], so for simplicity we neglect this potential frequency dependence, and report only frequency-independent t^* and Q. Additional discussion of frequency dependence, and equations to convert between frequency-independent and frequency-dependent Q values, can be found in *Stachnik et al.* [2004].

Previous studies have shown that spectral fitting methods assuming frequency independence of Q—such as ours—provide estimates of Q that are close to Q at the highest frequencies sampled if frequency dependence exists [*Stachnik et al.*, 2004]. This is presumably because signals are most sensitive to Q at the highest frequencies, where amplitudes are reduced the most. For these data, the highest frequencies are approximately 11–13 Hz, so Q estimates here should be considered to represent attenuation at those frequencies.

The mean t^* calculated for the entire data set is 0.055 ± 0.0025 s for P waves and 0.075 s ± 0.0034 s for S waves. Using a regionalization that divides our study area into a northern half and a southern half centered on 28.1°N, the mean t^* for P waves is 0.043 ± 0.0025 s beneath Nepal and 0.078 ± 0.0026 s beneath the Tibetan Plateau (Tethyan Himalaya). For S waves the variation is similar, 0.053 ± 0.0032 s under Nepal and 0.120 ± 0.0036 s beneath the Tibetan Plateau. Raypaths and path-averaged Q for a subset of the data are shown in Figure S2 in the supporting information. Regionally averaged crustal Q at depth can be estimated by separating near-surface attenuation (t^*_R) from path-averaged attenuation $1/Q$, by inverting

$$t*_n = t*_R + \left(\frac{\tau_n}{Q}\right) \tag{3}$$

for t^*_R and $(1/Q)$ from all measurements in a given region, where t^*_n is the t^* estimate from the nth raypath and τ_n is the corresponding travel time. The parameter t^*_R approximates attenuation contributions common

Table 1. Path-Averaged Q Estimates[a]

Event Depths	South Paths t^*_R (s)	± (s)	Q	North Paths t^*_R (s)	± (s)	Q
			P waves			
<50 km	0.024	0.002	1386	0.03	0.005	792
> 50 km	0.012	0.003	2280	0.025	0.007	493
			S waves			
< 50 km	0.048	0.003	5528	0.03	0.007	859
> 50 km	0.027	0.004	3145	0.086	0.022	519

[a]North/south path comparisons for t^*_R and Q calculated by regression for earthquakes at depths < 50 km and ≥ 50 km. Mean frequency bounds were 1.0–13.1 Hz for P and 0.7–11.2 Hz for S. Station RBSH (Figure 1) demarcates north versus south estimates.

to all paths in a region, such as near-surface effects [*Stachnik et al.*, 2004]. Results of this analysis are given in Table 1. We observe some differences between different regional subsets including that Q is higher for southern than northern paths (with the exception of Q_P for southern paths), and Q is lower for deeper events (indicating that Q decreases with increasing depth). In addition Q_P/Q_S is less than 1 for all regions.

4. Tomography

To better map out our observed variations in attenuation we invert the t^* estimates tomographically for 2-D Q variations in the crust and upper mantle. We focus on the variations in structure approximately normal to the Himalayan Arc and compare to a 2-D velocity model along this same transect [*Monsalve et al.*, 2008]. In order to compare the results of Q_P to Q_S, we use a subset of P and S wave spectra with common event-station paths. We assume the linear relationship between t^* and $1/Q$:

$$t*_n = \Sigma\tau_{nm}/Q_m \tag{4}$$

where t^*_n is the nth t^* observation, τ_{nm} is travel time determined from the 1-D velocity models of *Monsalve et al.* [2006] and $1/Q_m$ is attenuation in the mth block. We invert for $1/Q_m$ via truncated singular value decomposition using the algorithm of *Boyd et al.* [2004]. We experimented with different singular value truncations to optimize the variance reduction, resolution, and model variance, and in the final models retain singular values that are larger than 5% of the largest value. Inverse squared standard deviations of the t^* estimates from fits to equation (2) are used as the data weights, W.

We constructed the tomography for a 300 km (east–west) by 400 km (north–south) by 96 km (depth) volume centered at station RBSH (28.195°N, 86.828°E) (Figures 1 and S1). A two-dimensional inversion is performed to examine variations in attenuation parameters with latitude and with depth. Trade-off curves between misfit and model resolution show that the block dimensions that generate the greatest variance reduction with a high resolution are 40 km in the horizontal direction (north-south) and 24 km in the vertical direction. Using the sliding bin algorithm [*Boyd et al.*, 2004], we offset the blocks by 20 km in the horizontal and 12 km in the vertical and reran the inversion, for a total of four inversions. Results from the inversions are combined into one model, m_1. To test the sensitivity to raypaths, we ran the tomographic inversion for each phase (P and S) using two different input velocity models corresponding to different parts of the region [*Monsalve et al.*, 2006]. As a way to investigate ability to recover anomalies, we tested how well the data kernel matrix could reproduce a synthetic model with high attenuation blocks in the south and north (Figure 5). Approximately 82% of the synthetic model amplitude was recovered.

Patterns in the tomographic Q models (Figure 6) are consistent with attenuation variations observed from the path averages (Table 1). The obtained Q structures show little dependence on the velocity model used for ray tracing. Q_P and Qs show similar spatial variations, even though the data sets are independent and inverted separately, lending support to the robustness of the images.

The India crust beneath Nepal, including the Lesser Himalaya, shows low attenuation (Q_P and $Q_S \geq 2000$) with values from 500–1000 along the Main Himalayan Thrust (MHT). The middle to lower crust between the High

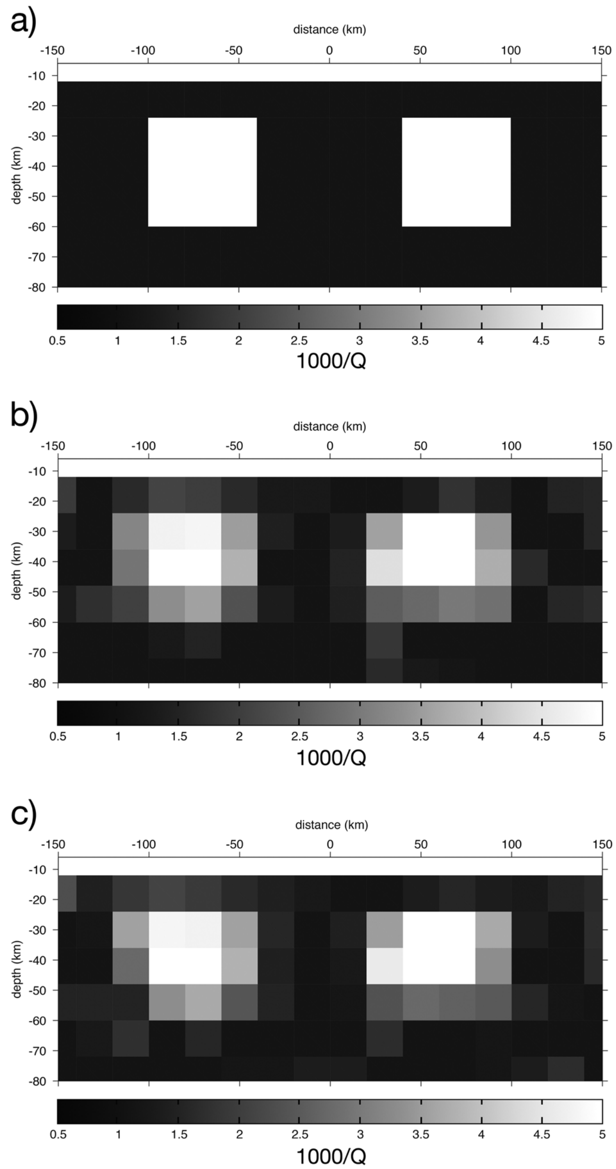

Figure 5. (a) Synthetic model of 1000/*Q* with high-attenuation blocks in the south (left) and north (right). (b) Recovery of synthetic model using *P* wave travel paths. (c) Recovery of synthetic model using *S* wave travel paths.

Himalaya and southern Tibetan Plateau shows relatively high attenuation (Q_P and $Q_S \leq 500$). The crust of the southern Tibetan Plateau at depths 20–60 km shows a high attenuation zone for *P* and *S* ($Q \approx 500$).

5. Discussion

We observe that *P* and *S* waves are significantly more attenuated as they pass through the crust beneath the High Himalaya and the southern Tibetan Plateau (Tethyan Himalaya) than signals that travel through the crust beneath the Lesser Himalaya and Ganges Plain. To the south, within the Lesser Himalaya, the greatest seismic wave attenuation (lowest Q_P and Q_S) is found along and within the footwall of the Main Himalayan Thrust (MHT). In the uppermost mantle beneath the high Himalaya, high Q_P and Q_S are found, and the region is brittle enough to produce earthquakes [*Monsalve et al.*, 2006]. The factor of 10 variations suggest a first-order influence of temperature variations, perhaps accompanied by melt. Our interpretations are illustrated in Figure 7. The variations in V_P/V_S from the velocity tomography of *Monsalve et al*. [2008] provide complementary information and are interpreted along with our attenuation models.

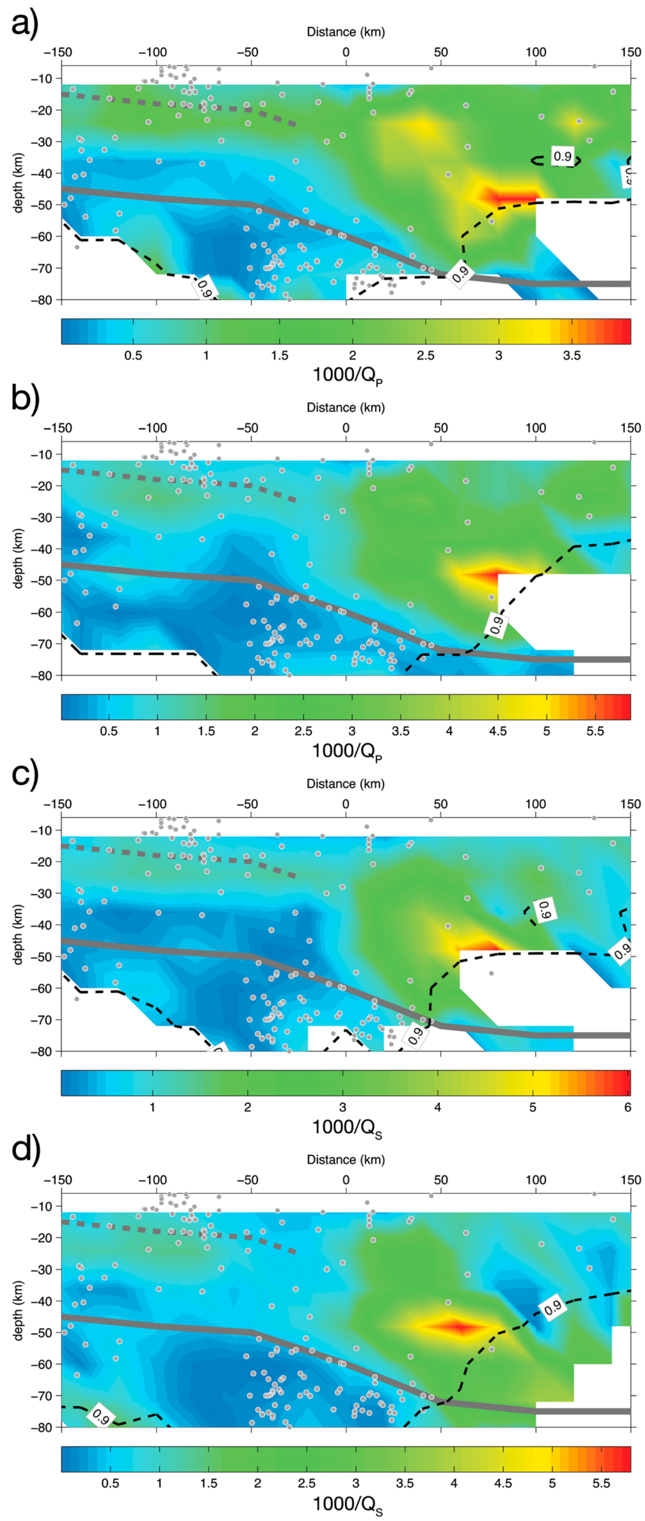

Figure 6. Tomographic 1000/*Q* cross sections at longitude 86.5°E. Center point of cross section is at latitude 28.1°N and south is left; (a) 1000/Q_P using the Nepal velocity model [*Monsalve et al.*, 2006]. See Figure S2 for ray coverage from deep earthquakes; (b) 1000/Q_P using the Tibet velocity model [*Monsalve et al.*, 2006]; (c) 1000/Q_S using the Nepal velocity model; (d) 1000/Q_S using the Tibet velocity model. Shallow-dashed line denotes the Main Himalayan Thrust (MHT), solid line denotes crust-mantle boundary (Moho) [*Schulte-Pelkum et al.*, 2005]. Black-dashed lines at depth indicate contours of 90% resolution. Earthquakes are denoted by grey circles.

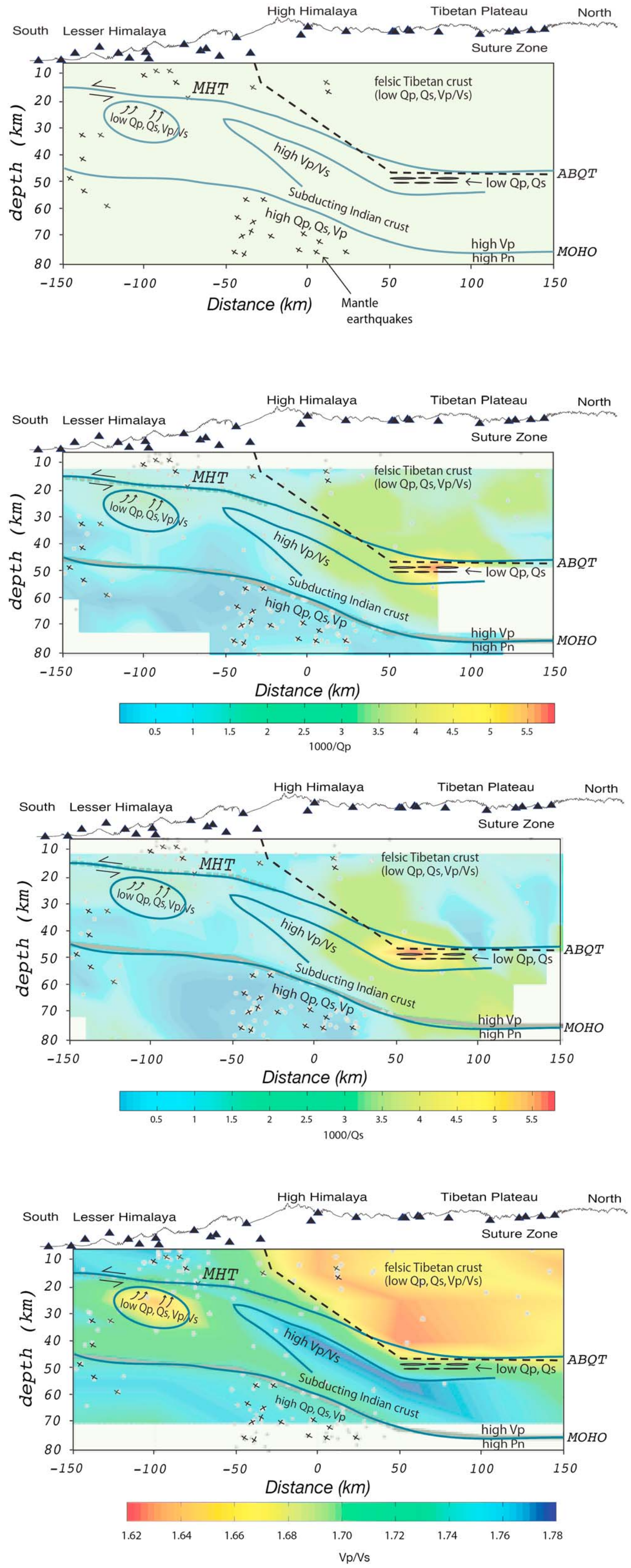

Figure 7. Interpretive view of north-south variations in $1000/Q_P$, $1000/\ Q_S$, and V_P/V_S. Topography along longitude 86.5°E is shown above each plot and black triangles denote projected HIMNT station locations. Center point of cross section is latitude 28.1°N and south is left. ABQT is alpha-beta quartz transition. (a) Interpretive diagram; (b) $1000/\ Q_P$; (c) $1000/\ Q_S$; (d) V_P/V_S from *Monsalve et al.* [2008].

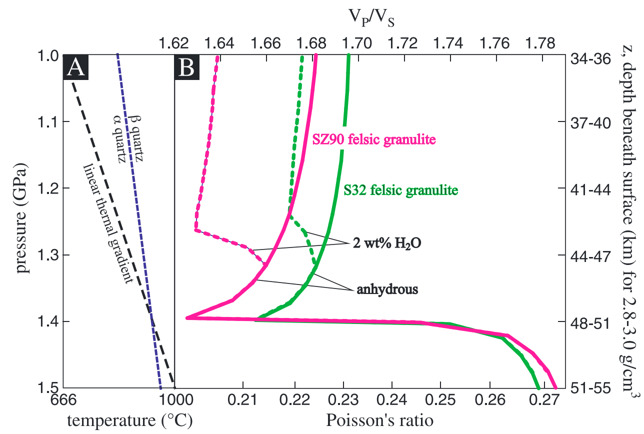

Figure 8. V_P/V_S versus depth for two felsic granulites. (a) Assumed thermal gradient and corresponding alpha-beta quartz transition of *Shen et al.* [1993]. (b) Calculated V_P/V_S ratio versus depth for two felsic granulites [from *Mahan*, 2006]. Velocities calculated using the algorithm of *Hacker and Abers* [2004].

Elevated temperature can greatly decrease *Q* [e.g., *Kampfmann and Berckhemer*, 1985; *Karato and Spetzler*, 1990]. Recent comparisons show similar attenuation-viscosity relationships for many materials [*McCarthy and Takei*, 2011; *McCarthy et al.*, 2011], and viscosity is strongly temperature-dependent for virtually all rock compositions [e.g., *Kohlstedt et al.*, 1995], so it is likely that attenuation is as well. Because calibrations of attenuation for crustal rocks remain incompletely understood, and bulk compositions are imperfectly known, we provide only qualitative interpretations on thermal structure; the effects of pore fluid and melt further complicate quantitative interpretations of *Q*.

Our favored interpretation for the low Q_P, low Q_S, and low V_P/V_S observed in the middle and upper crust of the Tethyan Himalaya is that it represents warm, felsic rock similar to that exposed in the Himalaya [*Bollinger et al.*, 2006; *Yin and Harrison*, 2000]. This interpretation is not only supported by the relatively low V_P/V_S ratio of 1.65 characteristic of quartz-rich rock [*Christensen*, 1996; *Monsalve et al.*, 2008] but also by high heat flow [*Jimenez-Munt et al.*, 2008; *Pollack et al.*, 1993]. These high temperatures are most likely sustained by radioactive heat generation in an unusually thick crustal section. The variations in *Q* that we observe correlate well with an independently determined model of temperature anomalies beneath the Himalaya and Tibet [*Wang et al.*, 2013].

We interpret the sharp increase in V_P/V_S ratio at 45 km below sea level (BSL) in the southern Tibetan crust as a result of the alpha to beta quartz transition (ABQT) in felsic crustal rocks. Laboratory studies [e.g., *Ohno et al.*, 2006] indicate that the ABQT at 1 atm is marked by a sharp increase in V_P/V_S ratio, and *Mechie et al.* [2004] have shown that the ABQT can be used as a crustal thermometer. In Figure 8, we show that typical felsic granulite compositions [*Mahan*, 2006] yield calculated isotropic V_P/V_S ratios that increase from ~1.68–1.70 in the alpha quartz stability field to ~1.78 in the beta quartz stability field for a linear thermal gradient from Earth's surface to 1.5 GPa and 1000°C. The velocities were calculated using the algorithm of *Hacker and Abers* [2004] with an updated database that includes new elastic data for alpha quartz at elevated temperature [*Lakshtanov et al.*, 2007; *Ohno et al.*, 2006], and elastic data at elevated pressure [*Calderon et al.*, 2007] assumed to scale with the pressure dependence of the ABQT. Phase abundances and compositions for the granulite were calculated with *Perple_X* [*Connolly and Petrini*, 2002] version 7, the 2004 version of the *Holland and Powell* [1998] database, and activity models in *Hacker* [2008], excluding melt.

For average crustal densities of 2800–3000 kg/m^3, an ABQT at 45 km BSL (50 km beneath the surface) corresponds to a pressure of 1400–1500 MPa; for the experimental determination of the ABQT of *Shen et al.* [1993] this corresponds to a temperature of 933–958°C, with an uncertainty of ~5°C if pressure is known; 930–960°C approximates this range. This high temperature in the midcrust is consistent with the inverted geotherm in temperature models [*Beaumont et al.*, 2004; *Cattin and Avouac*, 2000; *Craig et al.*, 2012; *Herman et al.*, 2010; *Wang et al.*, 2013] and, while warmer than the Nepal crust, demonstrates that the Southern Tibetan crust is cooler than the central Tibetan crust where the ABQT is shallower [*Mechie et al*., 2004] and xenoliths imply temperatures of 900–1100°C at 0.9–1.2 GPa [*Hacker et al*., 2000].

We find low crustal Q_P and Q_S values, less than 300 for frequency-independent measurements, at 45–50 km BSL within the southern Tibetan crust. Because the lowest *Q* patch ($<$ 200) is bounded above and below by higher *Q*, this attenuation anomaly can have a purely thermal origin only if there is a thermal maximum in the crust at this depth. Another possible source for the low *Q* at 45–50 km BSL is aqueous fluid ponded beneath the ABQT. Laboratory studies have shown that the transition from alpha to beta quartz at 1 atm is marked by an approximately threefold increase in porosity and permeability [*Glover et al*., 1995; *Lin*, 2002; *McKnight et al*., 2008]. Thus, the α-β quartz transition may act as a reservoir for fluid or melt, and the alpha quartz above it may form an impermeable cap. We speculate that the similar values for Q_S and Q_P reflect rough equivalence of processes that reduce shear modulus, such as diffusion-accommodated grain-boundary sliding [*Faul et al*., 2004], and dilatational anelasticity processes that affect the bulk modulus and thus V_P [*Green and Cooper*, 1993]. *Galvé et al*. [2006] also reported high attenuation in the lower crust of the Tibetan Plateau. Beyond the Himalayan orogen and Tibetan Plateau, the places that the ABQT can be observed in the Earth's crust may be few, as it requires thick, hot, felsic crust. A recent study by *Kuo-Chen et al*. [2012] reports evidence for the ABQT beneath the Central Range of Taiwan from V_P/V_S tomography, suggesting a high geothermal gradient beneath the orogen.

An unusual region of modestly high attenuation with low V_P/V_S (Figure 7) and high electrical conductivity [*Unsworth et al*., 2005] lies within the subducting Indian crust 20–30 km deep beneath the Lesser Himalaya. Aqueous fluids at high pore pressure might be a way to reconcile high electrical conductivity with low V_P/V_S [e.g., *Hauksson and Shearer*, 2006; *Makovsky and Klemperer*, 1999; *Matsubara et al*., 2004; *Nakajima et al*., 2001; *Sato and Ito*, 2002; *Toksoz et al*., 1979], because the relatively high compressibility of aqueous fluids relative to rock leads to rapid bulk modulus reduction with increasing porosity [*Takei*, 2002]. High porosity also can contribute to low Q_P and low Q_S [*Winkler and Nur*, 1979; *Winkler and Murphy*, 1995]. This mechanism is attractive for the modestly low *Q*, low V_P/V_S zone in the footwall of the Main Himalayan thrust, and may also play a role in the southern Tibetan crust. Such a region may be expected where subducting Indian crust undergoes dehydration metamorphic reactions that release fluids at pressures of 0.7–1 GPa. Its persistence suggests that such fluids do not migrate away rapidly.

We observe high values of Q_P and Q_S (low attenuation) in the uppermost mantle beneath the High Himalaya and the Tethyan Himalaya. Mantle earthquakes have also been observed in this region [*de la Torre et al*., 2007; *Monsalve et al*., 2006]. The high *Q* and presence of earthquakes is consistent with low temperatures and hence brittle conditions. The strong temperature dependence of *Q* is found largely at temperatures $>$ 950°C in olivine aggregates [*Faul and Jackson*, 2005] and corresponds to *Q* generally lower than observed here ($>$2000–4000, dominated by frequencies of 10–20 Hz). For frequencies of 15 Hz, a 1 mm grain size, and a pressure of 1.5 GPa, the model of Faul and Jackson predicts $Q_S >$ 2000 for olivine at temperatures $<$ 1080°C. We suspect that much higher Q_S is difficult to observe because other processes contribute to both intrinsic absorption and scattering, so at best the *Q* data provide an upper bound on temperature. The presence of seismicity at mantle depths probably requires significantly lower temperatures [e.g., *Scholz*, 1998]—less than 600°C if calibrations from oceanic mantle apply [*McKenzie et al*., 2005]. Still, the presence of the highest Q values here supports the idea from other observations that the Indian lithosphere remains cold beneath the Himalaya.

6. Summary and Conclusions

P and *S* waves crossing southern Tibet lose significant energy over short distances. Much of this attenuation is concentrated in the middle to lower crust beneath the High Himalaya and the southern Tibetan Plateau. At midcrustal depths a sharp increase in V_P/V_S corresponding to a patch of very high attenuation is interpreted as the alpha-beta quartz transition (ABQT) at 930–960°C. We interpret a patch of low Q_P and Q_S at 45–50 km depth as fluid trapped by the porosity and permeability contrast associated with the ABQT. Farther south, a region of moderately high attenuation but low V_P/V_S may represent a local zone of aqueous fluid produced by dehydration of subducting Indian crust. At greater depth, the combination of high *Q* for *P* and *S* waves beneath the Lesser Himalaya along with regions of high seismicity confirms that the upper mantle of the India Plate is cold and brittle.

Acknowledgments
This work was supported by National Science Foundation grants EAR-9903066, 0538259, and 1008760, and a Sloan Foundation Graduate Fellowship and the Montgomery G.I. Bill to T. de la Torre. We thank Oliver Boyd for providing the tomography algorithms and for guidance in their use. We thank the Department of Mines and Geology of Nepal and the Chinese Academy of Science for their assistance with the HIMNT field project, and the IRIS consortium for providing seismic equipment. Thanks to the HIMNT field team including F. Blume, R. Bendick, D. Huang, F. Wu, R. Bilham, S. Sapkota, S. Rajaure, U. Guatam, and V. Schulte-Pelkum. The Associate Editor and two anonymous reviewers provided input that led to significant improvements in the paper. Figure 1 was generated with the freely available Generic Mapping Tools (GMT) software [*Wessel and Smith*, 1991].

References

Aki, K., and P. G. Richards (2002), *Quantitative Seismology*, 2nd ed., Univ. Science Books, Sausalito, Calif.

Beaumont, C., R. A. Jamieson, M. H. Nguyen, and S. Medvedev (2004), Crustal channel flows: 1. Numerical models with applications to the tectonics of the Himalayan-Tibetan orogen, *J. Geophys. Res.*, *109*, B06406, doi:10.1029/2003JB002809.

Bollinger, L., P. Henry, and J. P. Avouac (2006), Mountain building in the Nepal Himalaya: Thermal and kinematic model, *Earth Planet. Sci. Lett.*, *244*(1–2), 58–71.

Boyd, O. S., and A. F. Sheehan (2005), Attenuation tomography beneath the Rocky Mountain Front: Implications for the physical state of the upper mantle, in *The Rocky Mountain Region: An Evolving Lithosphere*, pp. 361–377, AGU, Washington, D. C.

Boyd, O. S., C. H. Jones, and A. F. Sheehan (2004), Foundering lithosphere imaged beneath the southern Sierra Nevada, California, USA, *Science*, *305*(5684), 660–662.

Calderon, E., M. Gauthier, F. Decremps, G. Hamel, G. Syfosse, and A. Polian (2007), Complete determination of the elastic moduli of α-quartz under hydrostatic pressure up to 1 GPa: An ultrasonic study, *J. Phys. Condens. Matter*, *19*(43), 436,228, doi:10.1088/0953-8984/19/43/436228.

Caldwell, W. B., S. L. Klemperer, S. S. Ray, and J. F. Lawrence (2009), Partial melt in the upper-middle crust of the northwest Himalaya revealed by Rayleigh wave dispersion, *Tectonophysics*, *477*, 58–65.

Cattin, R., and J. P. Avouac (2000), Modeling mountain building and the seismic cycle in the Himalaya of Nepal, *J. Geophys. Res.*, *105*, 13,389–13,407.

Chen, W. P., and P. Molnar (1983), The depth distribution of intracontinental and intraplate earthquakes and its implications for the thermal and mechanical properties of the lithosphere, *J. Geophys. Res.*, *88*, 4183–4214.

Chen, W. P., and Z. Yang (2004), Earthquakes beneath the Himalayas and Tibet: Evidence for strong lithospheric mantle, *Science*, *304*, 1949–1952.

Christensen, N. I. (1996), Poisson's ratio and crustal seismology, *J. Geophys. Res.*, *101*, 3139–3156.

Clark, M. K., and L. H. Royden (2000), Topographic ooze: Building the eastern margin of Tibet by lower crustal flow, *Geology*, *22*(8), 703–706.

Connolly, J. A. D., and K. Petrini (2002), An automated strategy for calculation of phase diagram sections and retrieval of rock properties as a function of physical conditions, *J. Metamorph. Geol.*, *20*, 697–798.

Craig, T. J., A. Copley, and J. Jackson (2012), Thermal and tectonic consequences of India underthrusting Tibet, *Earth Planet. Sci. Lett.*, *353–354*, 231–239.

DeCelles, P. G., D. M. Robinson, J. Quade, T. P. Ojha, C. N. Garzione, P. Copeland, and B. N. Upreti (2001), Stratigraphy, structure, and tectonic evolution of the Himalayan fold-thrust belt in western Nepal, *Tectonics*, *20*, 487–509.

de la Torre, T. L., and A. F. Sheehan (2005), Broadband seismic noise analysis of the Himalayan Nepal Tibet Seismic Experiment, *Bull. Seismol. Soc. Am.*, *95*(3), 1202–1208.

de la Torre, T. L., G. Monsalve, A. F. Sheehan, S. Sapkota, and F. Wu (2007), Earthquake processes of the Himalayan collision zone in eastern Nepal and the southern Tibetan Plateau, *Geophys. J. Int.*, *171*, 718–738, doi:10.1111/j.1365-246X.2007.03537.x.

Faul, U. H., and I. Jackson (2005), The seimological signature of temperature and grain size variations in the upper mantle, *Earth Planet. Sci. Lett.*, *234*, 119–134.

Faul, U. H., J. D. Fitz Gerald, and I. Jackson (2004), Shear wave attenuation and dispersion in melt-bearing olivine polycrystals: 2. Microstructural interpretation and seismological implications, *J. Geophys. Res.*, *109*, B06202, doi:10.1029/2003JB002406.

Flanagan, M. P., and D. A. Wiens (1998), Attenuation of broadband *P* and *S* waves in Tonga: Observations of frequency dependent *Q*, *Pure Appl. Geophys.*, *153*, 345–375.

Galvé, A., M. Jiang, A. Hirn, M. Sapin, M. Laigle, B. de Voogd, J. Gallart, and H. Qian (2006), Explosion seismic *P* and *S* velocity and attenuation constraints on the lower crust of the North-Central Tibetan Plateau, and comparison with the Tethyan Himalayas: Implications on composition, mineralogy, temperature, and tectonic evolution, *Tectonophysics*, *412*(3–4), 141–157.

Gansser, A. (1964), *Geology of the Himalayas*, Wiley-Interscience, New York.

Glover, P. W. J., P. Baud, M. Darot, P. G. Meredith, S. A. Bonn, M. LeRavalec, S. Zoussi, and T. Reuschle (1995), α/β phase transition in quartz monitored using acoustic emissions, *Geophys. J. Int.*, *120*(3), 775–782.

Green, D. H., and R. F. Cooper (1993), Dilatational anelasticity in partial melts—Viscosity, attenuation, and velocity dispersion, *J. Geophys. Res.*, *98*, 19,807–19,817.

Hacker, B. R. (2008), H_2O subduction beyond arcs, *Geochem. Geophys. Geosyst.*, *9*, Q03001, doi:10.1029/2007GC001707.

Hacker, B. R., and G. A. Abers (2004), Subduction Factory 3: An Excel worksheet and macro for calculating the densities, seismic wave speeds, and H_2O contents of minerals and rocks at pressure and temperature, *Geochem. Geophys. Geosyst.*, *5*, Q01005, doi:10.1029/2003GC000614.

Hacker, B. R., E. Gnos, L. Ratcshbacher, M. Grove, M. McWilliams, S. V. Sobolev, W. Jiang, and Z. Wu (2000), Hot and dry xenoliths from the lower crust of Tibet, *Science*, *287*, 2463–2466.

Hauksson, E., and P. M. Shearer (2006), Attenuation models (Q_P and Q_S) in three dimensions of the southern California crust: Inferred fluid saturation at seismogenic depths, *J. Geophys. Res.*, *111*, B05302, doi:10.1029/2005JB003947.

Hazarika, P., M. R. Kumar, and D. Kumar (2013), Attenuation character of seismic waves in Sikkim Himalaya, *Geophys. J. Int.*, *195*, 544–557, doi:10.1093/gji/ggt241.

Herman, F., et al. (2010), Exhumation, crustal deformation, and thermal structure of the Nepal Himalaya derived from the inversion of thermochronological and thermobarometric data and modeling of the topography, *J. Geophys. Res.*, *115*, B06407, doi:10.1029/2008JB006126.

Hodges, K. V. (2000), Tectonics of the Himalaya and southern Tibet from two perspectives, *Geol. Soc. Am. Bull.*, *112*(3), 324–350.

Holland, J. B., and R. Powell (1998), An internally consistent thermodynamic data set for phases of petrological interest, *J. Metamorph. Geol.*, *16*, 309–343.

Jimenez-Munt, I., M. Fernandez, J. Verges, and J. P. Platt (2008), Lithosphere structure underneath the Tibetan Plateau inferred from elevation, gravity and geoid anomalies, *Earth Planet. Sci. Lett.*, *267*, 276–289.

Kampfmann, W., and H. Berckhemer (1985), High-temperature experiments on the elastic and anelastic behavior of magmatic rocks, *Phys. Earth Planet. Inter.*, *40*(3), 223–247.

Karato, S., and H. A. Spetzler (1990), Defect microdynamics in minerals and solid state mechanisms of seismic wave attenuation and velocity dispersion in the mantle, *Rev. Geophys.*, *28*, 399–421.

Klemperer, S. L. (2006), Crustal flow in Tibet: Geophysical evidence for the physical state of Tibetan lithosphere, and inferred patterns of active flow, in "*Channel Flow, Ductile Extrusion and Exhumation in Continental Collision Zones*", edited by R. D. Law, M. P. Searle, and L. Godin, *Geol. Soc. London Spec. Publ.*, *268*, 39–70.

Kohlstedt, D. L., B. Evans, and S. J. Mackwell (1995), Strength of the lithosphere: Constraints imposed by laboratory experiments, *J. Geophys. Res.*, *100*, 17,587–17,602, doi:10.1029/95JB01460.

Kuo-Chen, H., F. T. Wu, D. M. Jenkins, J. Mechie, S. W. Roecker, C.-Y. Wang, and B.-S. Huang (2012), Seismic evidence for the $\alpha-\beta$ quartz transition beneath Taiwan from *Vp/Vs* tomography, *Geophys. Res. Lett.*, *39*, L22302, doi:10.1029/2012GL053649.

Lakshtanov, D. L., S. V. Sinogeiken, and J. D. Bass (2007), High-temperature phase transitions and elasticity of silica polymorphs, *Phys. Chem. Miner.*, *34*(1), 11–22.

Larson, K., R. Burgmann, R. Bilham, and J. T. Freymueller (1999), Kinematics of the India-Eurasia collision zone from GPS measurements, *J. Geophys. Res.*, *104*, 1077–1093.

Lin, W. (2002), Permanent strain of thermal expansion and thermally induced microcracking in Inada granite, *J. Geophys. Res.*, *107*(B10), 2215, doi:10.1029/2001JB000648.

Madariaga, R. (1976), Dynamics of an expanding circular fault, *Bull. Seismol. Soc. Am.*, *65*, 163–182.

Mahan, K. (2006), Retrograde mica in deep crustal granulites: Implications for crustal seismic anisotropy, *Geophys. Res. Lett.*, *33*, L24301, doi:10.1029/2006GL028130.

Makovsky, Y., and S. L. Klemperer (1999), Measuring the seismic properties of Tibetan bright spots: Evidence for free aqueous fluids in the Tibetan middle crust, *J. Geophys. Res.*, *104*, 10,795–10,825, doi:10.1029/1998JB900074.

Matsubara, M., N. Hirata, H. Sato, and S. Sakai (2004), Lower crustal fluid distribution in the northeastern Japan arc revealed by high-resolution 3D seismic tomography, *Tectonophysics*, *388*(1–4), 33–45.

McCarthy, C., and Y. Takei (2011), Anelasticity and viscosity of partially molten rock analogue: Toward seismic detection of small quantities of melt, *Geophys. Res. Lett.*, *38*, L18306, doi:10.1029/2011GL048776.

McCarthy, C., Y. Takei, and T. Hiraga (2011), Experimental study of attenuation and dispersion over a broad frequency range: 2. The universal scaling of polycrystalline materials, *J. Geophys. Res.*, *116*, B09207, doi:10.1029/2011JB008384.

McKenzie, D., J. Jackson, and K. Priestley (2005), Thermal structure of oceanic and continental lithosphere, *Earth Planet. Sci. Lett.*, *233*, 337–349.

McKnight, R. E. A., T. Moxon, A. Buckley, P. A. Taylor, T. W. Darling, and M. A. Carpenter (2008), Grain size dependence of elastic anomalies accompanying the α-β phase transition in polycrystalline quartz, *J. Phys. Condens. Matter*, *20*, 075,229, doi:10.1088/0953-8984/20/7/075229.

Mechie, J., S. V. Sobolev, L. Ratschbacher, A. Y. Babeyko, G. Bock, A. G. Jones, K. D. Nelson, K. D. Solon, L. D. Brown, and W. Zhao (2004), Precise temperature estimation in the Tibetan crust from seismic detection of the $\alpha-\beta$ quartz transition, *Geology*, *32*(7), 601–604, doi:10.1130/G20367.1.

Mitchell, B. J. (1995), Anelastic structure and evolution of the continental crust and upper mantle from seismic surface-wave attenuation, *Rev. Geophys.*, *33*, 441–462.

Molnar, P. (1984), Structure and tectonics of the Himalaya: Constraints and implications of geophysical data, *Annu. Rev. Earth Planet. Sci.*, *12*, 489–518.

Monsalve, G., A. Sheehan, V. Schulte-Pelkum, S. Rajaure, M. R. Pandey, and F. Wu (2006), Seismicity and one-dimensional velocity structure of the Himalayan collision zone: Earthquakes in the crust and upper mantle, *J. Geophys. Res.*, *111*, B10301, doi:10.1029/2005JB004062.

Monsalve, G., A. Sheehan, C. Rowe, and S. Rajaure (2008), Seismic structure of the crust and the upper mantle beneath the Himalayas: Evidence for eclogitization of lower crustal rocks in the Indian Plate, *J. Geophys. Res.*, *113*, B08315, doi:10.1029/2007JB005424.

Morozov, I. B. (2009), Thirty years of confusion around "scattering *Q*"?, *Seismol. Res. Lett.*, *80*, 5–7.

Nakajima, J., T. Matsuzawa, and A. Hasegawa (2001), Three-dimensional structure of *Vp*, *Vs* , and *Vp/Vs* beneath northeastern Japan: Implications for arc magmatism and fluids, *J. Geophys. Res.*, *106*, 21,843–21,857, doi:10.1029/2000JB000008.

Nelson, K. D., et al. (1996), Partially molten middle crust beneath southern Tibet: Synthesis of project INDEPTH results, *Science*, *274*(5293), 1684–1688.

Ohno, I., K. Harada, and C. Yoshitomi (2006), Temperature variation of elastic constants of quartz across the alpha-beta transition, *Phys. Chem. Miner.*, *33*(1), 1–9.

Park, J., C. R. Lindberg, and F. L. Vernon (1987), Multitaper spectral-analysis of high-frequency seismograms, *J. Geophys. Res.*, *92*, 12,675–12,684.

Pollack, H. N., S. J. Hurter, and J. R. Johnson (1993), Heat flow from the Earth's interior: Analysis of the global data set, *Rev. Geophys.*, *31*, 267–280, doi:10.1029/93RG01249.

Priestley, K., J. Jackson, and D. McKenzie (2008), Lithospheric structure and deep earthquakes beneath India, the Himalaya and southern Tibet, *Geophys. J. Int.*, *172*, 345–372.

Robinson, D. M., P. G. DeCelles, C. N. Garzione, O. N. Pearson, T. M. Harrison, and E. J. Catlos (2003), Kinematic model of the Main Central Thrust in Nepal, *Geology*, *31*(4), 359–362.

Sato, H., and K. Ito (2002), Olivine-pyroxene-H_2O system as a practical analogue for estimating the elastic properties of fluid-bearing mantle rocks at high pressures and temperatures, *Geophys. Res. Lett.*, *29*(9), 1325, doi:10.1029/2001GL014212.

Scholz, C. H. (1998), Earthquakes and friction laws, *Nature (London)*, *391*(6662), 37–42.

Schulte-Pelkum, V., G. Monsalve, A. Sheehan, M. R. Pandey, S. Sapkota, R. Bilham, and F. Wu (2005), Imaging the Indian subcontinent beneath the Himalaya, *Nature*, *435*(7046), 1222–1225.

Sheehan, A. F., et al. (2008), Earthquakes and crustal structure of the Himalaya from the Himalayan Nepal Tibet Seismic Experiment (HIMNT), *J. Nepal Geol. Soc.*, *38*, 1–8.

Shen, A. H., W. A. Bassett, and I. M. Chou (1993), The alpha-beta quartz transition at high temperatures and pressures in a diamond-anvil cell by laser interferometry, *Am. Mineral.*, *78*(7–8), 694–698.

Singh, C., A. Singh, V. K. Bharathi, A. R. Bansal, and R. K. Chadha (2012), Frequency-dependent body wave attenuation characteristics in the Kumaun Himalaya, *Tectonophysics*, *524–525*, 37–42, doi:10.1016/j.tecto.2011.12.013.

Stachnik, J. C., G. A. Abers, and D. H. Christensen (2004), Seismic attenuation and mantle wedge temperatures in the Alaska subduction zone, *J. Geophys. Res.*, *109*, B10304, doi:10.1029/2004JB003018.

Takei, Y. (2002), Effect of pore geometry on V_P/V_S: From equilibrium geometry to crack, *J. Geophys. Res.*, *107*(B2), 2043, doi:10.1029/2001JB000522.

Toksoz, M. N., D. H. Johnston, and A. Timur (1979), Attenuation of seismic waves in dry and saturated rocks: I. Laboratory measurements, *Geophysics*, *44*(4), 681–690, doi:10.1190/1.144096.

Unsworth, M. J., A. G. Jones, W. Wei, G. Marquis, S. G. Gokarn, and J. E. Spratt (2005), Crustal rheology of the Himalaya and southern Tibet inferred from magnetotelluric data, *Nature*, *438*(7064), 78–81.

Wang, C. Y., W. P. Chen, and L. P. Wang (2013), Temperature beneath Tibet, *Earth Planet. Sci. Lett.*, *375*, 326–337, doi:10.1016/j.epsl.2013.05.052.

Wessel, P., and W. H. F. Smith (1991), Free software helps map and display data, *Eos Trans. AGU*, *72*, 441.
Winkler, K. W., and W. F. Murphy (1995), Acoustic velocity and attenuation in porous rocks, in *Rock Physics & Phase Relations: A Handbook of Physical Constants*, edited by T. J. Ahrens, pp. 20–34, AGU, Washington, D. C.
Winkler, K. W., and A. Nur (1979), Pore fluids and seismic attenuation in rocks, *Geophys. Res. Lett.*, *6*, 1–4.
Yin, A., and T. M. Harrison (2000), Geologic evolution of the Himalayan-Tibetan orogen, *Annu. Rev. Earth Planet. Sci.*, *28*, 211–280.
Zhao, W. J., K. D. Nelson, and Project INDEPTH Team (1993), Deep seismic reflection evidence for continental underthrusting beneath southern Tibet, *Nature*, *366*(9), 557–559.